11.2 A Numerical Study of Clear-Air Turbulence (CAT) Encounters Occurred in Korea

Jung-Hoon Kim and Hye-Yeong Chun*

Department of Atmospheric Sciences, Yonsei University, Seoul, South Korea.

1. Introduction

Clear-air turbulence (CAT) is defined as the bumps of in-flight aircraft directly induced by small-scale turbulent eddies in free atmosphere within cloud free or stratiform clouds (Ellord et al. 2003). In the aviation industry, incidents of CAT remain serious concerns because they usually occur unexpectedly at dominant flight altitudes of commercial aircraft, which results in damage such as occupant injuries, fuel losses, and flight delays. As air transportation has increased, the importance of CAT forecasting has increased (Sharman et al. 2006). To develop more useful CAT forecasting skills and to assist pilots in avoiding CAT, it is essential to investigate and understand possible mechanisms of individual CATs through numerical simulations (Lane et al. 2003; Lane and Sharman 2008).

Large portions of CATs have been explained by Kelvin-Helmholtz instability (hereafter KHI), which is triggered when the local Richardson number ($Ri_g = N^2/VWS^2$, where N and VWS are the Brunt-Vaisala frequency and vertical wind shear, respectively) is less than 0.25 in a stably stratified shear flow (Howard 1961; Miles 1961). Under this condition, turbulent kinetic energy increases by extracting energy from the mean flow and eventually cascades down to smaller scale eddies, which typically have scales similar to the aircraft (Sekioka 1970; Joseph et al. 2004). In the real atmosphere, CATs induced by KHI frequently occur above or below the jet stream where the VWS is sufficiently strong to overcome its environmental stability. In addition, the entrance region of the jet stream and the confluence zone of two different flows favor CAT generation through upper-level frontogenesis (Mancuso and Endlich 1966; Roach 1970). However, it is not sufficient to describe highly localized individual CATs sorely by using KHI based on frontogenesis (Knox 1997; Ellord and Knox 2009).

CATs occurring in anticyclonic flow have been considered as the important portion of total CATs, even though their frequency is not as high as those in cyclonic flows. Knox (1997) showed that total deformation induced by upper-level frontogenesis is not reliable to explain the CATs in strong anticyclonic flow. Rather, inertial instability and/or geostrophic adjustment could be regarded as the source of the CATs in the strong anticyclonic flow. Clark et al. (2000) demonstrated that the location of severe turbulence over Colorado on 9 December 1992 is consistent with the region of observed and simulated horizontal vortex tubes (HVTs). Combining the afore-mentioned concepts from Knox (1997) and Clark et al. (2000), Kaplan et al. (2005) suggested a forecasting index, the North Carolina State University index 2 (NCSU2 = $\nabla\zeta\times\nabla M$, where ζ and M are streamwise vertical vorticity and

* *Corresponding author address*: Prof. Hye-Yeong Chun, Department of Atmospheric Sciences, Yonsei University, 262 Seongsanno, Seodaemun-gu, Seoul, 120-749, South Korea; E-mail: chunhy@yonsei.ac.kr

Montgomery streamfunction on an isentrophic surface, respectively), and showed that the NCSU2 index is maximized in a region where the strong gradient of the streamwise vertical vorticity is perpendicular to the strong pressure gradient force at an isentrophic surface, which finally transits to the HVTs and causes localized turbulence. Another mechanism for CATs is breakdown of gravity waves generated by complex terrains. Jiang and Doyle (2004), Doyle et al. (2005), and Lane et al. (2009) claimed that large-amplitude mountain waves and their subsequent breaking over complex terrain are responsible for small-scale turbulence that directly affects aircraft.

Climatologically, the region around the Korean peninsula and Japan has a stronger jet stream than any other regions of the world during all seasons. For this reason, potential CAT encounters diagnosed using several CAT indices are relatively high in East Asia including in Korea, as shown by Jaeger and Sprenger (2007). In addition, the Korean peninsula is covered mostly (more than 70%) by complex structures of topography as shown in Fig. 1, so that the prevailing westerly flows over Korea can produce mountain waves with a wide spectrum. In these circumstances, the aforementioned generation mechanisms can be applied to the observed CATs in Korea.

The remainder of this paper is organized as follows. In section 2, observation of nine MOG-level CATs over Korea on 2 April 2007 is described. In section 3, the experimental setting of the WRF model is given. In section 4, synoptic features simulated by the WRF model and assimilated in the Regional Data Assimilation and Prediction System (RDAPS) provided by the Korea Meteorological Administration (KMA) are described. In section 5, generation mechanisms for nine MOG-level CATs occurred in the three different regions are investigated in detail. Summary and conclusions are given in the last section.

2. Investigation of CAT encounters

On 2 April 2007, twelve turbulence encounters were reported in PIREPs over South Korea and nine of them were the MOG-level CATs, which occurred during the 6.5 hrs from 0200 (1100) to 0830 (1730) UTC (LST). Considering that the average number of PIREPs per day is 3.4 and the number of CATs among the PIREPs is less than two per day in Korea for the last 10 years (Kim and Chun 2008), the occurrence of twelve PIREPs and twelve CATs with nine MOG-level CATs in a day is very unusual. The atmospheric condition over the Korean peninsula during this period might be sufficiently vulnerable to generate aircraft turbulence. In the present study, we will investigate exclusively the nine MOG-level CATs (CATs hereafter refers to those nine MOG-level CATs). Time, latitude, longitude, flight level in km, and turbulence intensity of the CATs are presented in Table 1, and their horizontal distribution is depicted in Fig. 1. As shown in Fig. 1, CATs are distributed in three regions: west coast, Jeju Island, and eastern mountain areas of Korea. These three areas are indicated by W, J, and E in Table 1, respectively. Table 1 shows that most of the CATs occurred in the 3 hrs from 0530 to 0830 UTC, except for the first one which occurred at 0200 UTC. All CATs over the west coast area occurred within ±1 hour of 0700 UTC. CATs over Jeju Island and the eastern mountain areas have more time gaps between individual CATs. Among the reported altitudes, turbulence levels near the west coast area are relatively lower (Z = 5 - 8 km) than in the other two regions (Z = 9 - 13 km). Among the nine CATs, eight of them are in moderate intensity and the one that occurred at

0530 UTC near Jeju Island is a severe-level CAT.

Because PIREPs usually do not clarify whether they are CATs or in-cloud turbulence, to identify the existence of clouds during this period, composite images of the Multi-functional Transport SATellite (MTSAT) focused on Korea and East Asia are used (Fig. 2). In Fig. 2a, there are no clouds over the west coast and the eastern mountain areas in the Korean peninsula, while stratiform clouds that expand from South China cover Jeju Island. In Fig. 2b, many clouds and cloud bands are located along the surface frontal system that extends from South China to South Japan, and some portions of them extend to Jeju Island. There are no signals of precipitation in radar echoes or at the surface observation stations in Korea including on Jeju Island on 2 April 2007 (not shown). For these reasons, turbulences occurred in Korea during this period are regarded as CATs.

3. Experimental design of WRF model

The numerical model used in this study is the WRF model version 3.0 developed at the National Center for Atmospheric Research (NCAR), which is a non-hydrostatic and fully compressible model. Details of this model can be found in Skamarock et al. (2008). This model has been used for several previous studies on turbulence (e.g., Feltz et al. 2008; Fovell et al. 2007; Passner and Knapp 2008; Trier and Sharman 2009) and gravity waves (e.g., Plougonven et al. 2008; Kim et al. 2009). Locations of all model domains used in the present simulation are shown in Fig. 3. Six domains are considered in the present simulation with horizontal grid spacings of 30, 10, 3.3, 1.1, 1.1, and 0.37 km in domains 1, 2, 3, 4, 5, and 6, respectively. The locations of domains for the first three (domains 1, 2, and 3) and the last three (domains 4, 5, and 6) are depicted in Fig. 3a and Fig. 3b, respectively. Two-way nesting interactions are conducted for domains 1 and 2, 2 and 3, 3 and 4, and 3 and 5, while one-way interaction is conducted for domains 5 and 6.

All domains have 87 vertical layers with a vertical resolution of about 300 m and a model top of 20 hPa. A sponge layer with Rayleigh damping is included in the uppermost 7 km to prevent an artificial reflection. Lateral boundary layers are specified with 5 relaxation grids in each domain. For initial and boundary conditions, reanalysis data from the National Centers for Environmental Prediction (NCEP) at 6 hr interval and 1° grid spacing in latitude and longitude (Derber et al. 1991) are used. The integrations were conducted for 24 hrs from 1200 UTC 1 to 1200 UTC 2 April 2007 in domains 1 and 2 and for 18 hrs from 1800 UTC 1 to 1200 UTC 2 April 2007 in domains 3 to 6.

The parameterizations used in the present simulation include the cloud microphysics scheme by Hong and Lim (2006), the land-surface scheme by Chen and Dudhia (2001), the Mellor-Yamada-Janjic planetary boundary layer (MYJ PBL) scheme by Janjic (2002), the short wave radiation scheme by Dudhia (1989), and the long wave radiation scheme by Malwer et al. (1997). The cumulus parameterization scheme by Kain (2004) is used exclusively in domains 1 and 2. Note that the MYJ PBL scheme takes into account vertical mixing not only in PBL but in the free atmosphere by calculating sub-grid turbulent kinetic energy to third order accuracy. Therefore, sub-grid scale turbulence in the CAT regions can be parameterized by the MYJ PBL scheme without considering any additional turbulence scheme in the upper troposphere.

4. Synoptic-scale flow

In this section, the synoptic-scale flow pattern around the Korean peninsula on 2 April 2007 as it

appeared in the RDAPS analysis data is described, and a comparison with the simulated results in the 30 km domain (domain 1) is conducted. Figure 4 shows horizontal distributions of wind speed superimposed on geopotential height at 300 hPa level (Fig. 4a) and sea-level pressure (Fig. 4b) from the RDAPS analysis (left) and the WRF simulation results (right) at 0000 UTC 2 April 2007. At this time, the jet stream flows from the west to the east over the Korean peninsula with a maximum speed of 74 m s^{-1}. In addition, a highly curved trough in the entrance region of the jet core approaches the Korean peninsula. Also, the pressure-gradient force across the Korean peninsula is exceptionally strong on 2 April 2007 due to an intensified Siberian high at the surface. The simulated results are fairly good compared with the RDAPS analysis in both wind and sea-level pressure fields.

For further investigation of synoptic structure and comparison between the model result and observation, vertical profiles of wind and temperature derived from the simulation in domains 1 to 3 are compared with those observed from two radiosonde stations denoted by the stars in Fig. 3b. Because the simulated soundings in the three domains are similar, only the result in domain 1 will be discussed and compared with the observation. Figure 5 shows the skew *T*-log *p* diagrams of temperature, dew-point temperature, and wind derived using the simulated (gray lines) and the observed (black lines) soundings at (a) Baekryung-do and (b) Gwangju at 0000 UTC 2 April 2007. Relatively strong stabilities in the layer between Z = 4 and 8 km at Baekryung-do and between Z = 3 and 5 km at Gwangju stations are observed. This intensified stability in the mid troposphere is related to the subsidence of stratospheric air due to deep tropopause folding. Details of the tropopause folding will be presented in section 5a. In addition, the maximum wind speed of 82 (63.5) m s^{-1} is located at 334 (253) hPa [about Z = 9 (10.4) km] at Baekryung-do (Gwangju) station, hence strong VWS below the maximum wind appears between Z = 4 and 8 km at both stations. The height range of the enhanced VWS is very similar to that of the CATs occurred over the west coast area of Korea on 2 April 2007. The model captures the aforementioned vertical structures of the observation reasonably well, although with some discrepancies between the simulation and observation.

5. Model results

a. West coast area

The potential temperatures in domain 2 at Z = 6.1 km (average level of No. 3, 4, and 6 CATs) at 1800 UTC 01 (left) and 0700 UTC 2 April 2007 (right) are shown in Fig. 6a, and horizontal wind speed at Z = 9 km (the level of the maximum jet stream) superimposed with horizontal wind vectors and pressure at Z = 6.1 km are shown in Fig. 6b. Intensifying upper-level front and associated jet stream are identified during this 13 hrs. At 1800 UTC, a relatively strong meridional temperature gradient in a frontal zone is located from the Balhae bay to the northern part of the Korean peninsula. As this frontal zone moves southward, the meridional temperature gradient increases at 0700 UTC (Fig. 6b), implying an intensified upper-level front during this period. As the strengthening frontal zone induces strong VWS through the thermal-wind relationship, the maximum wind speed of the jet core above the frontal zone also increases from 70.2 m s^{-1} to 82.9 m s^{-1} over the 13 hrs. In addition, the convergence zone south-westerlies in the entrance region of the jet core ahead of the highly curved trough approaches the west coast of Korea, where the No. 3, 4, and 6

CATs occurred (Fig. 6b).

In order to understand how localized turbulences are related to the evolution of the intensifying upper-level front/jet system, we show in Fig. 7 the horizontal wind speed (Fig. 7a) and Richardson number (Fig. 7b) superimposed with potential temperature and 1.5 PVU (potential vorticity unit) in Y-Z cross sections along the line shown in Fig. 6b (right), using the same data shown in Fig. 6. At 1800 UTC (Fig. 7a; left), the jet core is located at Z = 9 km and the maximum wind speed there is 74 m s^{-1}. The upper-level front represented by slantwise and dense contours of the potential temperature in the mid troposphere near Z = 3 - 6 km and Y = 600 - 1200 km is located below the jet core and has relatively strong vertical and horizontal gradients of wind speed and temperature, respectively. In addition, the height of the dynamic tropopause (1.5 PVU) decreases from its background height of about Z = 10-12 km on the anticyclonic side of the jet core to about Z = 5 km on the cyclonic side of the jet core following the upper-level front. At 0700 UTC (Fig. 7b; right), the overall structure of the upper-level front/jet system is similar to that at 1800 UTC. However, the slope of the isentropes near the upper-level front is steeper, so the jet maximum at Z = 9 km becomes larger (89 m s^{-1}). In addition, the tropopause is deeply folded down to about Z = 4 km with a steep 1.5 PVU line following the upper-level front. Because of this deep tropopause folding, relatively strong stability layers are located in the mid troposphere due to the intrusion of relatively stable stratospheric air. This is consistent with the observation profiles of the temperature shown in Fig. 5. As the development of the upper-level front/jet system causes strong horizontal temperature gradient in the upper-level frontal zone, VWS is maximized through the thermal wind relationship. Consequently, the local Richardson number becomes smaller along this frontal zone mainly due to strong VWS regardless of strong stability (see Fig. 7b). The locations and timings of the No. 3, 4, and 6 CATs observed on the west coast of Korea are reproduced reasonably well in domain 2 of the simulation.

To investigate the resolution dependency of the simulation results illustrated in Fig. 7b (right), Y-Z cross-sections of the Richardson number superimposed with the potential temperature and 1.5 PVU in the different domains are presented in Fig. 8. Figure 8a, b, and c are the simulated results from domain 1 (ΔX = 30 km), domain 2 (ΔX = 10 km), and domain 3 (ΔX = 3.3 km) in the region occupied by two vertically dashed lines shown in Fig. 7b (right), respectively. Overall features of the tropopause folding and upper-level frontal system are similar, except that the lines of 1.5 PVU become steeper as horizontal grid resolution becomes higher. These regions of small Richardson number are sustained for about 5 hours from 0400 UTC to 0900 UTC, during which the intensifying upper-level front/jet system is dominant over the Korean peninsula. The smallest Richardson number is 0.224 near the location of the No. 4 CAT in domain 3. In all three domains, the regions of the small Richardson number are not obviously different, implying no significant resolution dependency on the simulation results in this area. The simulation with 30 km horizontal grid spacing can identify regions of the CATs sufficiently in this area at this time.

b. Jeju Island

In Fig. 7b (right), a region of relatively low static stability (relatively sparse contours of potential temperature) and small Richardson number is located on the anticyclonic shear side of the jet core near Z = 7 - 10 km and Y = 300 - 600 km. Three CATs, the No. 2, 8, and 9 CATs,

observed over the Jeju Island area are located in this region at this time in domain 2 (Fig. 9). This region has relatively strong horizontal wind shear, but weak VWS [vertically oriented contours of isotach; see Fig. 7b (right)]. In some local regions on the anticyclonic side of the jet core, the local Richardson number is less than zero, implying that there exist local vertical mixings of potential temperature in Fig. 9.

Figure 10a shows the accumulated convective precipitation superimposed with zero absolute vorticity (s^{-1}), horizontal wind vector, and pressure at the 10.7 km level (averaged level of the No. 2, 8, and 9 CATs over the Jeju Island area) derived using the simulated results of domain 1 at 1900 UTC 01 (left) and 0800 UTC 02 (right). Note that Fig. 10a is not the whole area of domain 1, but focuses on the regions of anticyclonic flow and the Jeju Island area. Note also that the absolute vorticity enclosed by the zero lines is negative. During this period, the Jeju Island area is located in the anticyclonic shear side of the jet core, which is passing through the west coast of Korea as described in the previous section. Because of this strong anticyclonic shear flow, areas of negative absolute vorticity increase during this period (Fig. 10a). Considering that the inertial instability associated with the negative absolute vorticity has been regarded as a possible source of local turbulence that directly affects aircraft in the anticyclonic flow (Knox 1997; McCann 2001; Trier and Sharman 2009), CATs observed in the Jeju Island area are likely related to the inertial instability.

As the upper-level front/jet system is intensified during this period, the maximized wind speed of the jet core causes the anticyclonic shear region (negative absolute vorticity) to be larger near the Jeju Island area (Fig. 10a, right). On top of that, ageostrophic flow is also dominant, which can be seen from the largely different angle between the wind vectors and isobaric lines. This strong ageostrophic flow may be caused by well-developed convection systems in the southern part of China, as seen by accumulated convective precipitation in Fig. 10a (right). As dominant westerly flow passes through the developed convection system, wind vectors are significantly perturbed and distorted on the lee-side of the convective system (Fig. 10a, right). As locally enhanced cross-streamwise confluent flow (ageostrophic flow) forms the local maximum of the vertical component of relative vorticity (vertical vorticity hereafter) in this anticyclonic shear side of the jet core region, local concentration of vertical vorticity causes perturbations of absolute vorticity. As a result, zero contours of absolute vorticity are also perturbed (Fig. 10a, right). Assuming that strong horizontal gradients of vertical vorticity can be translated to a micro-scale horizontal vortex tube (Clark et al. 2000; Kaplan et al. 2005), this could generate small-scale turbulence that directly affects aircraft. As can be seen in Fig. 10a (right), the region of perturbations of zero absolute vorticity along the maximized streamwise-oriented gradient of vertical vorticity is consistent with the location of the No. 2, 8, and 9 CATs over the Jeju Island area.

Figure 10b shows zonal cross-sections of the NCSU2 index superimposed with zero absolute vorticity along the dashed line shown in Fig. 10a. The NCSU2 index is maximized where the vectors between the pressure gradient force and the gradient of streamwise vorticity become orthogonal, in contrast to geostrophic flow where those become parallel. At 1900 UTC 01, local vertical mixings or relatively strong values of the NCSU2 index do not exist in this cross-section, even though the negative absolute vorticity region is located in the eastern part of China. As the

upper-level front/jet system intensifies and the dominant westerly flow starts to be disturbed as it passes through the well-developed convective system at 0800 UTC 02, local vertical mixings occurs near Z = 9 - 11 km and X = 2500 - 3000 km. These regions are well matched with the regions of the maximized NCSU2 index between Z = 6 and 11 km and X = 2500 and 3300 km. This maximized NCSU2 is highly correlated with the negative absolute vorticity region, which is induced by ageostrophic convergent flow on the anticyclonic shear side of the jet core as shown in Fig. 10a. The regions of relatively large values of NCSU2 are also consistent with the local maximum of subgrid-scale turbulent kinetic energy (TKE), which will be shown in Fig. 11. As a result, both model diagnosed turbulence potential and subgrid-scale TKE capture reasonably well the regions of CATs over the Jeju Island area.

In order to identify the resolution dependency of the simulated results illustrated in Fig. 9, Y-Z cross-sections of subgrid-scale TKE superimposed with potential temperature and zero contours of absolute vorticity are shown in Fig. 11, using the simulated results in domains 1 to 3 shown in the dashed box in Fig. 9. Overall features of the subgrid-scale TKE and potential temperature are similar in each domain. The maximum subgrid-scale TKE (1.212 $m^2 s^2$) occurs at the location of the No. 2 CAT in domain 3, while it is less close to the No. 2 CAT in domain 1. In all domains, the regions of local vertical mixing induced by ageostrophically disturbed flow in the anticyclonic shear side of the jet core are not obviously different. This suggests that numerical simulation even with 30 km horizontal grid spacing can identify the regions of CATs in this area at this time. In addition, the modeled turbulence in this area is maintained for about 5 hours from 0400 UTC to 0900 UTC in domains 1, 2, 3, and 4 (not shown). This is because the environmental conditions conducive to the CATs continue in this area when the synoptic or mesoscale forcings support their generation.

c. Eastern mountain area

To precisely simulate mountain waves generated by complex terrain, topography and large-scale flow have to be represented realistically. This is because characteristics of the mountain waves such as amplitude and wave length are highly dependent on the structure of topography as well as upstream wind and stability. For this reason, an additional domain, domain 6 (ΔX = 0.37 km), is included in domain 5 (ΔX = 1.1 km) of the eastern mountain area, as shown in Fig. 3b, with one-way nesting interaction. Initial conditions and physical parameterizations in domains 5 and 6 are the same as those in the coarser domains, but the boundary conditions in domain 6 are from the results of domain 5 updated every 30 minutes.

Figure 12 shows vertical velocity (shading) superimposed on horizontal wind vectors in domain 3 at four different levels (Z = 15, 11, 7, and 3 km) at 0300 UTC 02. In this figure, localized wave structure is captured over the eastern side of South Korea. These waves are generated by the strong zonal flow across the meridionally oriented mountains over the eastern part of the Korean peninsula. In particular, their amplitudes near the locations of the No. 1, 5, and 7 CATs over the eastern mountain area are larger than other regions at Z = 11 km, with the maximum amplitude of vertical velocity of +3.0 and -4.4 m s^{-1} near the location of the No. 7 CAT. This shows clearly that smaller-scale waves appear more in the lower altitudes, while only relatively long-wavelength components reach up to the upper troposphere.

In order to understand the filtering process of

the short-wavelength waves at low altitude, the vertical profile of m^2 (where m is the vertical wavenumber) for a stationary mountain wave is calculated using the following equation.

$$m^2 = \frac{N^2}{U^2} - \frac{1}{U^2}\frac{d^2U}{dz^2} - k^2.$$

Here k is the horizontal wavenumber, and U and N are the basic-state wind and Brunt-Vaisala frequency, respectively. Figure 13 shows m^2 profiles of waves with horizontal wavelengths of 12.5 km (Fig. 13a) and 4.2 km (Fig. 13b). The U and N profiles used to calculate m^2 are the domain-averaged (domain 6) zonal wind and temperature at 0300 UTC 2 April 2007. The vertical wavenumber of the stationary gravity waves for a given horizontal wavelength changes with altitude as the background stability and wind change. Once a vertically propagating gravity wave meets a level of m^2 = 0, it can be reflected backward from the reflection level (level of m^2 = 0) (Gossard and Hooke, 1975). In Fig. 13, significant reduction in m^2 appears between Z = 4 and 8 km due to the existence of strong variance in background stability in the troposphere, which is mainly due to the deep tropopause foldings as mentioned in section 5a. There is no level of m^2 = 0 for the gravity wave with a relatively longer horizontal wavelength (12.5 km; Fig. 13a), while a deep evanescent layer exists (Z = 5.2 - 10.6 km) for the wave with short horizontal wavelength (4.2 km; Fig. 13b). For the given U and N used in Fig. 13, we found that waves with horizontal wavelengths shorter than 10.5 km can be reflected in the 4 - 8 km height range. Thus, smaller-scale waves appear more in the lower altitudes, while only relatively long-wavelength components reach up to the upper troposphere, as shown in Fig. 12.

Figure 14 shows X-Z cross-sections of the Richardson number (Fig. 14a) and subgrid-scale TKE superimposed with potential temperature (Fig. 14b), zonal wind (Fig. 14c), and vertical velocity (Fig. 14d) in domain 6 at 0300 UTC 02 along the line of Y = 75 km in domain 6 (36.86º N in Fig. 12) at which the No. 7 CAT is located. Zero and negative values of the wind component are depicted as bold and dashed lines in Figs. 14c and Fig. 14d, respectively. It shows that mountain waves simultaneously break down in Z = 13.5 - 17 km. This breaking activates subgrid-scale TKE in that region (Fig. 14b). However, the simulated turbulence is located above the observed No. 7 CAT. This discrepancy will be examined in Fig. 17. Between Z = 3 and 5 (5 and 9) km, a relatively strong (lower) stability layer appears, and this is likely due to the deep tropopause foldings, as shown in Fig. 7. In Fig. 14c, the maximum zonal wind that exceeds 70 m s^{-1} locates near Z = 8 km. However, the zonal wind decreases with height above about Z = 10 km and zero wind regions appear near Z = 15 km. The zero wind is derived from the breaking of the gravity waves, and it becomes a wave-induced critical level (WICL) of the stationary mountain wave (Clark and Peltier 1984). Once the WICL is formed, consecutive stationary mountain waves can be either reflected from or absorbed at the critical level, depending on the local Richardson number. Since the local Richardson number is lower than 0.25 near the WICL (Fig. 14a), mountain waves are likely to be reflected at WICL.

Figure 14 demonstrated clearly that there exist regions of wave breaking in the 13.5 - 17 km height range, and this can generate local turbulence. However, the simulated wave-breaking regions are located somewhat higher than the location of the observed No. 7 CAT. In order to understand the factors that create the discrepancy, we performed an additional simulation with a different subgrid-scale turbulence scheme, the

YSU PBL scheme (Noh et al. 2003; Hong et al. 2006), in domain 6 through one-way nesting to domain 5 that used the MYJ PBL scheme. The simulated turbulence near the No. 7 CAT using YSU PBL in domain 6, however, is not evidently different from that using the MYJ PBL scheme (not shown). This implies that simulated turbulence in domain 6 is not very sensitive to the choice of subgrid-scale turbulence scheme. Rather, simulated variables, such as wind and temperature fields, that are important to determine the wave-breaking condition can be different from the observation, and consequently, the simulated wave-breaking height is higher than the observed height. To examine this possibility, we estimated the wave-breaking height from the mountain-drag parameterization by Chun et al. (1996) based on Palmer et al. (1986), using the basic-state wind and stability profiles obtained from the simulation and observation. Following is a brief description of how to estimate the wave-breaking height from Chun et al. (1996): (i) calculate mountain-wave stress at the surface (denoted by subscript s) $\tau_s = -K_0 \rho_s N_s U_s \left| h' \right|^2$, where K_0 is horizontal wavenumber (2.85×10^{-4} corresponding to 22 km horizontal wavelength is used), ρ_s is air density, N_s is Brunt-Vaisala frequency, U_s is the basic-state wind, and h' is the subgrid-scale topography height (300 m is used). (ii) calculate height variation due to the gravity wave at any level using $(\delta h)_k = \left\{ \left| \tau_{k-1} \right| / \left(K_0 \rho_{k-1} N_{k-1} U_{k-1} \right) \right\}^{1/2}$. (iii) find wave-breaking level based on the minimum Richardson number including wave effect $[Ri_m = Ri(1-\varepsilon)/(1+\varepsilon Ri^{1/2})^2]$, where *Ri* is the local Richardson number and ε is treated as the Froude number $[\varepsilon = (\delta h)_k N_{k-1} / U_{k-1}]$. If Ri_m < 1/4, wave breaking occurs and the saturation wave stress is calculated. If $Ri_m \geq 1/4$, there is no wave breaking and wave stress is the same as that at the level below. (iv) repeat this step at higher levels until the wave stress is zero or the model or observation top is reached.

Figure 15 shows vertical profiles of the basic-state wind (Fig. 15a), Brunt-Vaisala frequency (Fig. 15b), minimum Richardson number (Fig. 15c), and mountain-wave stress (Fig. 15d) derived using the simulated result in domain 6 (solid) and an observed rawinsonde sounding at Osan (dashed) at 0000 UTC 02 April, 2007. Osan is located in the upstream of the eastern mountain area and is depicted in Fig. 3b. The model-produced basic-state wind and Brunt-Vaisala frequency are obtained from the zonal-mean zonal wind and temperature in the cross-section shown in Fig. 14. The observed basic-state wind and Brunt-Vaisala frequency are derived by applying a nine-point vertical average to the rawinsonde data. The simulated basic-state wind and stability resembles the observation in a reasonable sense, except with relatively weak vertical variation and different magnitude. Because of this discrepancy, vertical profiles of the minimum Richardson number differ significantly for the simulated and the observed. Based on the simulated basic-state flow, the first wave breaking occurs at Z = 14 km, which is consistent with the altitude of the simulated turbulence shown in Fig. 14. In contrast, the wave-breaking height estimated using the observed basic-state flow in the upper troposphere is 12.8 km, and it is close to the altitude of the observed No. 7 CAT (12.6 km). Detailed inspection of the simulated and observed wind and stability near 12 to 14 km reveals that a slight difference in the vertical variation and magnitude of the basic-state flow causes a difference in the wave-breaking height of more than 1 km.

5. Summary and conclusions

On 2 April 2007, nine MOG-level CATs were reported in PIREPs during 6.5 hrs over the Korean peninsula. This is the highest number of CAT occurrences in one day for the last 10 years. These CATs were distributed in three different regions; the west coast, Jeju Island, and the eastern mountain areas of Korea. In the composite images from the MTSAT satellite, there are no clouds over the west coast and eastern mountain areas, while the Jeju Island area is covered with stratiform clouds expending from the southern part of China. Based on the available observations such as radar reflectivity and record of precipitations, all CATs including those in Jeju Island occurred in the clear weather.

The characteristics and possible generation mechanisms of the CATs in the three areas are investigated using available observations and simulation results of the WRF model, including six nested domains with the finest horizontal grid spacing of 0.37 km. Large-scale features simulated in the lowest-resolution domain (ΔX = 30 km) resemble those appeared in the RDAPS analysis data with the same resolution. In addition, vertical profiles of the temperature, dew-point temperature, and wind direction and speed derived from the simulation match reasonably well with those of the radiosonde observations.

Based on the simulation results, we found that generation mechanisms for CATs in the three regions are somewhat different. In the west coast area, an intensifying upper-level frontal zone is formed by strong meridional temperature gradient through the thermal wind relationship, and upper-level frontogenesis causes strengthening of the jet stream over the west coast area, which finally introduces maximized vertical wind shear below the jet core. Deep tropopause folding on the cyclonic shear side of the jet core leads to local Richardson number being smaller than 0.25, which can trigger Kelvin-Helmholtz instability. The locations of the KHI are consistent with those of the observed MOG-level CATs over the west coast area. Resolution dependency of the simulated turbulence in this area is not significant, and even the result with 30 km horizontal grid spacing and 300 m vertical grid spacing can identify the regions of the CATs during this period.

CATs observed in the Jeju Island area are likely associated with inertial instability. As the intensifying upper-level front/jet system approaches the Korean peninsula, the region of inertial instability becomes larger and moves to the Jeju Island area in the anticyclonic shear side of the maximized jet core. As strong westerly flows passing through a well-developed convective system become disturbed, ageostrophically induced mesoscale disturbance causes strong horizontal gradient of local vertical vorticity in the lee-side of the convective system. This results in the local vertical mixings at Z = 9 - 11 km that directly affects aircraft scale turbulence in the Jeju Island area. Simulations with 30 and 10 km horizontal grid spacings with 300 m vertical grid spacing can detect this turbulence with reliable timing and location.

In the eastern mountain area, CATs are associated with breaking of the mountain waves in the lower stratosphere. As air density decreases with height, the amplitudes of the mountain waves become larger above the jet core, and subsequently, mountain waves break down in a local area and lead to turbulence. Local turbulence due to subsequent wave breaking over the steepest mountain area is identified and reproduced in the simulation result with the finest domain (ΔX = 0.37 km), even though the altitude of the simulated turbulence is somewhat higher

than the observation. To figure out the reasons for the altitude discrepancy, the height of the No. 7 CAT over the eastern mountain area is estimated using a mountain-wave parameterization with the observed and simulated soundings. The results show that a slight difference in the basic-state wind and stability between the simulation and observation near the CAT cause a significant discrepancy in the altitudes of the turbulence (more than 1 km).

Although there exist several discrepancies in the location and timing of individual CATs between simulation and observation, the generation mechanisms of the observed CATs in different regions are reasonably well represented in the present simulations using the WRF model. To advance our understanding of localized turbulence in the East Asia region, more CAT cases that occurred under various conditions need to be investigated. In addition, like other regions of frequent turbulence occurrence, such as the Alps (Jiang and Doyle 2004), Greenland (Doyle et al. 2005; Lane et al. 2009), and the Pacific ocean (Lane et al. 2004; Koch et al. 2005), observational experiments including aircraft measurements over Korea and East Asia may be needed to understand the mechanisms of CAT generation and to improve CAT forecasting.

ACKNOWLEDGMENTS: This work was supported by the Korea Research Foundation Grant funded by the Korean Government (MOEHRD, Basic Research Promotion Fund) (KRF-2007-313-C00778).

REFERENCES

Chen, F., and J. Dudhia, 2001: Coupling an advanced land surface/hydrology model with the Penn State-NCAR MM5 modeling system. *Mon. Wea. Rev.*, **129**, 569-585.

Chun, H.-Y., J.-H. Jung, J.-H. Oh, and J.-W. Kim, 1996: Effects of mountain-induced gravity wave drag on atmospheric general circulation. *J. Kor. Meteor. Soc.*, **32**, 581-591.

Clark, T. L., and W. R. Peltier, 1984: Critical level reflection and the resonant growth of nonlinear mountain waves. *J. Atmos. Sci.*, **41**, 3122-3134.

_____, W. D. Hall, R. M. Kerr, D. Middleton, L. Radke, F. M. Ralph, P. J. Nieman, and D. Levinson, 2000: Origins of aircraft damaging clear air turbulence during the 9 December 1992 Colorado downslope windstorm. *J. Atmos. Sci.*, **57**, 1105-1131.

Derber, J. C., D. F. Parrish, and S. J. Lord, 1991: The global operational analysis system at the National Meteorological Center. *Wea. Forecasting*, **6**, 538-547.

Doyle, J. D., M. A. Shapiro, Q. Jiang, and D. L. Bartels, 2005: Large-amplitude mountain wave breaking over Greenland. *J. Atmos. Sci.*, **62**, 3106-3126.

Dudhia, J., 1989: Numerical study of convective observed during the winter monsoon experiment using a meso-scale two-dimensional model. *J. Atmos. Sci.*, **46**, 3077-3107.

Ellrod, G., and D. Knapp, 1992: An objective clear-air turbulence forecasting technique: Verification and operational use. *Wea. Forecasting*, **7**, 150-165.

_____, P. F. Lester, and L. J. Ehernberger, 2003: Clear air turbulence. *In Encyclopedia of Atmospheric Sciences*, vol. 1, J. R. Holton et al. (eds), Academic Press, 393-403.

_____, and J. A. Knox, 2009: Improvements to an operational clear air turbulence diagnostic index by addition of a divergence trend term. *Wea. Forecasting*, (in press).

Feltz, W. F., J. A. Otkin, K. M. Bedka, S. A.

Ackerman, A. Wimmers, R. D. Sharman, and J. R. Mecikalski, 2008: Satellite-derived mountain wave turbulence interest field detection. Preprints, *13th Conf. on Aviation, Range, and Aerospace Meteorology*, New Orleans, LA, Amer. Meteor. Soc., 9.3A.

Fovell, R. G., R. D. Sharman, and S. B. Trier, 2007: A case study of convectively-induced clear air turbulence. Preprints, *12th Conf. on Mesoscale Processes*, Waterville Valley, NH, Amer. Meteor. Soc., 13.4.

Gossard, E. E., and W. H. Hooke, 1975: *Waves in the Atmosphere*. Elsevier, Amsterdam, 456 pp.

Hong, S.-Y., and J.-O. J. Lim, 2006: The WRF single-moment 6-class microphysics scheme (WSM6). *J. Korean Meteor. Soc.*, **42**, 129-151.

_____, Y. Noh, and J. Dudhia, 2006: A New vertical diffusion package with an explicit treatment of entrainment processes. *Mon. Wea. Rev.*, **134**, 2318-2341.

Howard, L. N., 1961: Note on a paper by John Miles. *J. Fluid Mech.*, **10**, 509-512.

Jaeger, E. B., and M. Sprenger, 2007: A Northern hemispheric climatology of indices for clear air turbulence in the tropopause region derived from ERA40 reanalysis data. *J. Geo. Res.*, **112**, D20106, doi:10.1029/ 2006JD008189.

Janjic, Z. I., 2002: Nonsingular implementation of the Mellor-Yamada level 2.5 scheme in the NCEP meso model. *NCEP office note*, No. 437, 61 pp.

Jiang, Q., and J. D. Doyle, 2004: Gravity wave breaking over the central Alps: Role of complex terrain. *J. Atmos. Sci.*, **61**, 2249-2266.

Joseph, B., A. Mahalov, B. Nicolaenko, and K. L. Tse, 2004: Variability of turbulence and its outer scales in a model tropopause jet. *J. Atmos. Sci.*, **61**, 621-643.

Kain, J. S., 2004: The Kain-Fritsch convective parameterization: An update. *J. Appl. Meteor.*, **43**, 170-181.

Kaplan, M. L., A. W. Huffman, K. M. Lux, J. D. Cetola, J. J. Charney, A. J. Riordan, Y.-L. Lin, and K. T. Waight III, 2005: Characterizing the severe turbulence environments associated with commercial aviation accidents. Part 2: Hydrostatic mesoscale numerical simulations of supergradient wind flow and streamwise ageostrophic frontogenesis. *Meteor. Atmos. Phys.*, **88**, 129-153.

Keller, J. L., 1990: Clear air turbulence as a response to meso- and synoptic-scale dynamic processes. *Mon. Wea. Rev.*, **118**, 2228-2242.

Kim, J.-H., and H.-Y. Chun, 2008: Analysis on the spatial and temporal distribution of the aircraft turbulences occurred in South Korea for the recent 10 years. Preprints, *13th Conf. on Aviation, Range, and Aerospace Meteorology*, New Orleans, LA, Amer. Meteor. Soc., P3.3.

Kim, S.-Y., H.-Y. Chun, and D. Wu, 2009: A Study on stratospheric gravity waves generated by typhoon Ewinia: Numerical simulations and satellite observations. *J. Geophys. Res.* (in press).

Knox, J. A., 1997: Possible mechanism of clear-air turbulence in strongly anticyclonic flow. *Mon. Wea. Rev.*, **125**, 1251-1259.

_____, D. W. McCann, and P. D. Williams, 2008: Application of the Lighthill-Ford theory of spontaneous imbalance to clear-air turbulence forecasting. *J. Atmos. Sci.*, **65**, 3292-3304.

Lane, T. P., R. D. Sharman, T. L. Clark, and H.-M. Hsu, 2003: An investigation of turbulence generation mechanisms above deep convection. *J. Atmos. Sci.*, **60**, 1297-1321.

_____, and R. D. Sharman, 2008: Some influences of background flow conditions on the generation of turbulence due to gravity wave breaking above deep convection. *J. Appl. Meteor.*, **47**, 2777-2796.

_____, J. D. Doyle, R. D. Sharman, M. A. Shapiro, and C. D. Watson, 2009: Statistics and dynamics of aircraft encounters of turbulence over Greenland. *Mon. Wea. Rev.*, 137, 2687-2702.

Lilly, D. K., 1978: A severe downslope windstorm and aircraft turbulence event induced by a mountain wave. *J. Atmos. Sci.*, **35**, 59-77.

Malwer, E. J., S. J. Taubman, P. D. Brown, M. J. Iacono, and S. A. Clough, 1997: Radiative transfer for in-homogeneous atmospheres: RRTM, a validated correlated-k model for the longwave. *J. Geophys. Res.*, **102**, 16663-16682.

Mancuso, R. L., and R. M., Endlich, 1966: Clear air turbulence frequency as a function of wind shear and deformation. *Mon. Wea. Rev.*, **94**, 581-585.

Miles, J. W., 1961: On the stability of heteorogeneous shear flows. *J. Fluid Mech.*, **10**, 496-508.

Noh, Y., W. G. Cheon, S.-Y. Hong, and S. Raasch, 2003: Improvement of the K-profile model for the planetary boundary layer based on large eddy simulation data. *Bound.-Layer Meteor.*, **107**, 401-427.

Palmer, T. N., G. J. Shutts, and R. Swinbank, 1986: Alleviation of a systematic westerly bias in general circulation and numerical weather prediction models through an orographic gravity wave drag parameterization. *Quart. J. Roy. Meteor. Soc.*, **112**, 1001-1039.

Passner, J. E., and D. I. Knapp, 2008: Using WRF-ARW data to forecast turbulence at small scales. Preprints, *13th Conf. on Aviation, Range, and Aerospace Meteorology*, New Orleans, LA, Amer. Meteor. Soc., P3.1.

Plougonven, R., A. Hertzog, and H. Teitelbaum, 2008: Observations and simulations of a large-amplitude mountain wave breaking over the Antarctic Peninsula. *J. Geophys. Res.*, **113**, D16113, doi:10.1029/2007JD009739.

Roach, W. T., 1970: On the influence of synoptic development on the production of high level turbulence. *Quart. J. Roy. Meteor. Soc.*, **96**, 413-429.

Schwartz, B., 1996: The quantitative use of PIREPs in developing aviation weather guidance products. *Wea. Forecasting*, **11**, 372-384.

Sekioka, M., 1970: Application of Kelvin-Helmholtz instability to clear air turbulence. *J. Appl. Meteor.*, **9**, 896-899.

Sharman, R., C. Tebaldi, G. Wiener, and J. Wolff, 2006: An integrated approach to mid- and upper- level turbulence forecasting. *Wea. Forecasting*, **21**, 268-287.

Skamarock, W. C., J. B. Klemp, J. Dudhia, D. O. Gill, D. M. Barker, M. G. Duda, X.-Y. Huang, W. Wang, and J. G. Powers, 2008: A description of the advanced research WRF version 3. NCAR technical note, NCAR/TN-475+STR.

Table 1. Time, latitude, longitude, flight level, and intensity of nine MOG (moderate-or-greater)-level CATs over Korea reported in PIREPs on 2 April 2007. E, J, and W in the first column indicate the three categorized regions: west coast, eastern mountain, and Jeju Island of Korea, respectively. Flight levels (km) in the fifth column are calculated using the corresponding standard atmospheric height above ground level (AGL) from the pressure records provided by conventional PIREPs.

Number	Time (UTC)	Latitude (°N)	Longitude (°E)	Flight level (km)	Turbulence Intensity
1 (E)	0200	37.08	129.78	11.8	Moderate
2 (J)	0530	33.21	126.48	10.9	Severe
3 (W)	0600	36.80	126.69	7.2	Moderate
4 (W)	0700	37.78	125.70	5.8	Moderate
5 (E)	0730	36.20	129.23	12.2	Moderate
6 (W)	0750	37.58	126.17	5.0	Moderate
7 (E)	0800	36.86	129.46	12.6	Moderate
8 (J)	0810	32.43	125.73	10.8	Moderate
9 (J)	0830	33.61	126.98	9.8	Moderate

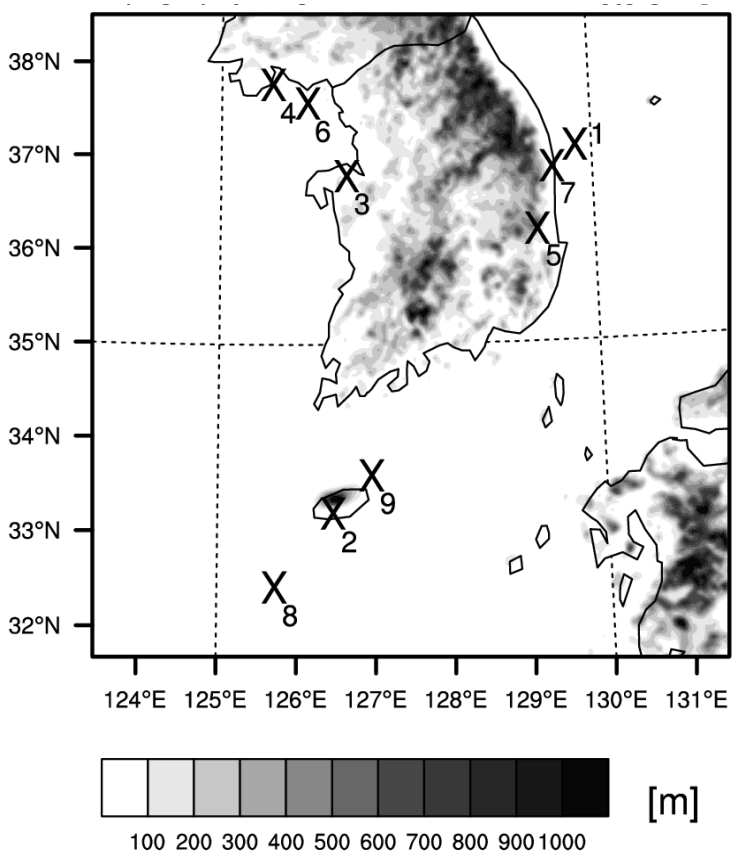

Fig. 1. Locations of MOG-level CATs occurred in Korea on 2 April 2007 superimposed with terrain height (shadings). The numbers of individual CATs correspond to those described in Table 1.

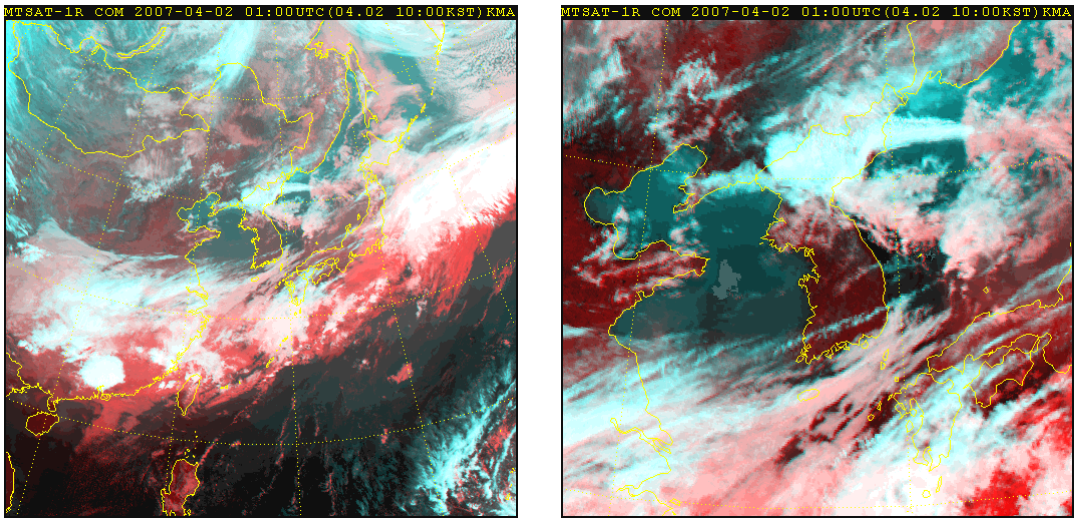

(a) **(b)**

Fig. 2. Composite images of the Multi-functional Transport SATellite (MTSAT) focused in (a) East Asia and (b) Korea at 0100 UTC 2 April 2007.

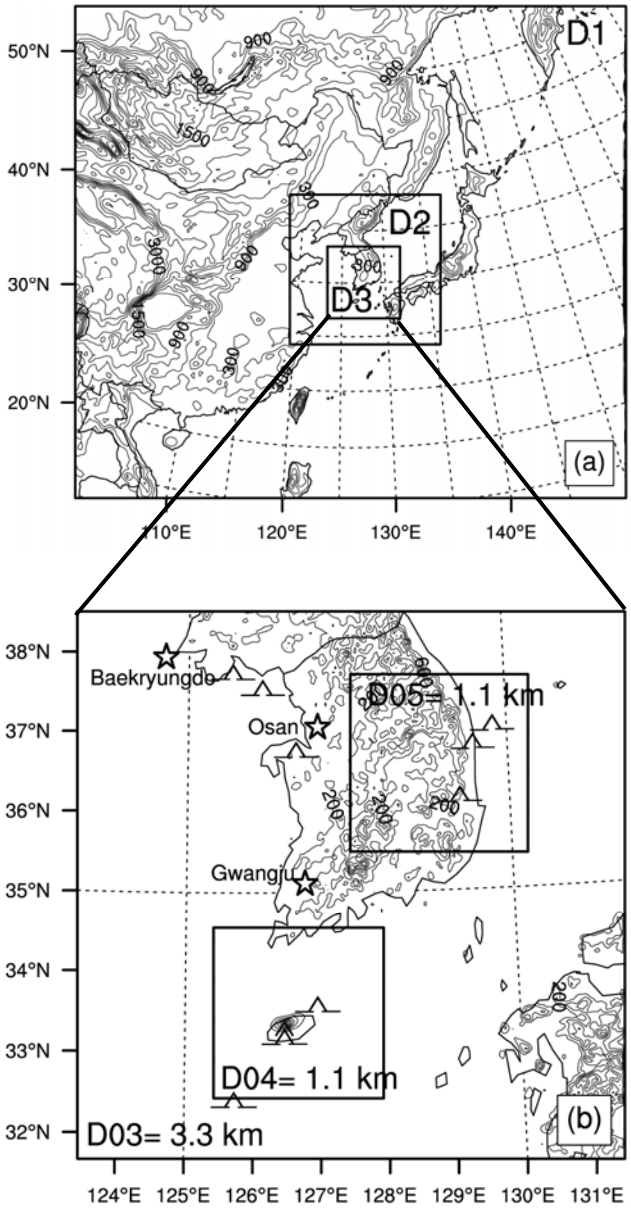

Fig. 3. Horizontal locations of (a) the first three domains (domain 1; ΔX = 30 km, domain 2; ΔX = 10 km, and domain 3; ΔX = 3.3 km) superimposed with terrain height (contour interval of 300 m) of domain 1 and (b) the last four domains (domain 3, domain 4; ΔX = 1.1 km, domain 5; ΔX = 1.1 km, and domain 6; ΔX = 0.37 km) superimposed with terrain height (contour interval of 200 m) of domain 3. Locations of nine MOG-level CATs and three radiosonde stations (Baekryungdo, Osan, and Gwangju) are depicted with the traditional marks of turbulence intensities and the stars with site name, respectively.

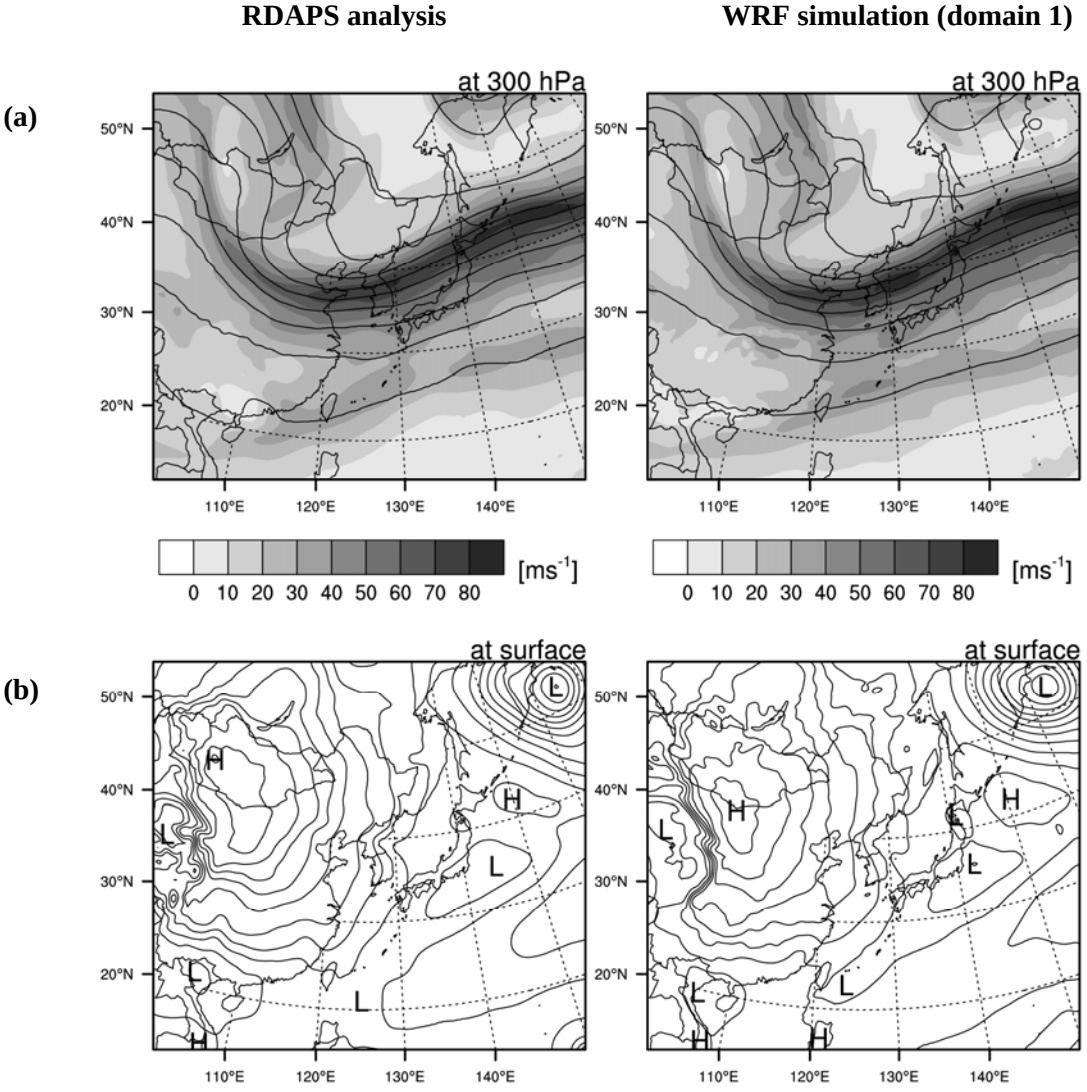

Fig. 4. (a) Horizontal wind speed (shading) superimposed with geopotential height (contour) at 300 hPa and (b) sea-level pressure (contour) at 00 UTC 2 April 2007 from the Regional Data Assimilation and Prediction System (RDAPS) 30 km analysis data provided by the Korea Meteorological Administration (KMA) (left) and WRF (Weather Research Forecast) model output of domain 1 (right). Contour intervals of (a) and (b) are 60 gpm and 4 hPa, respectively.

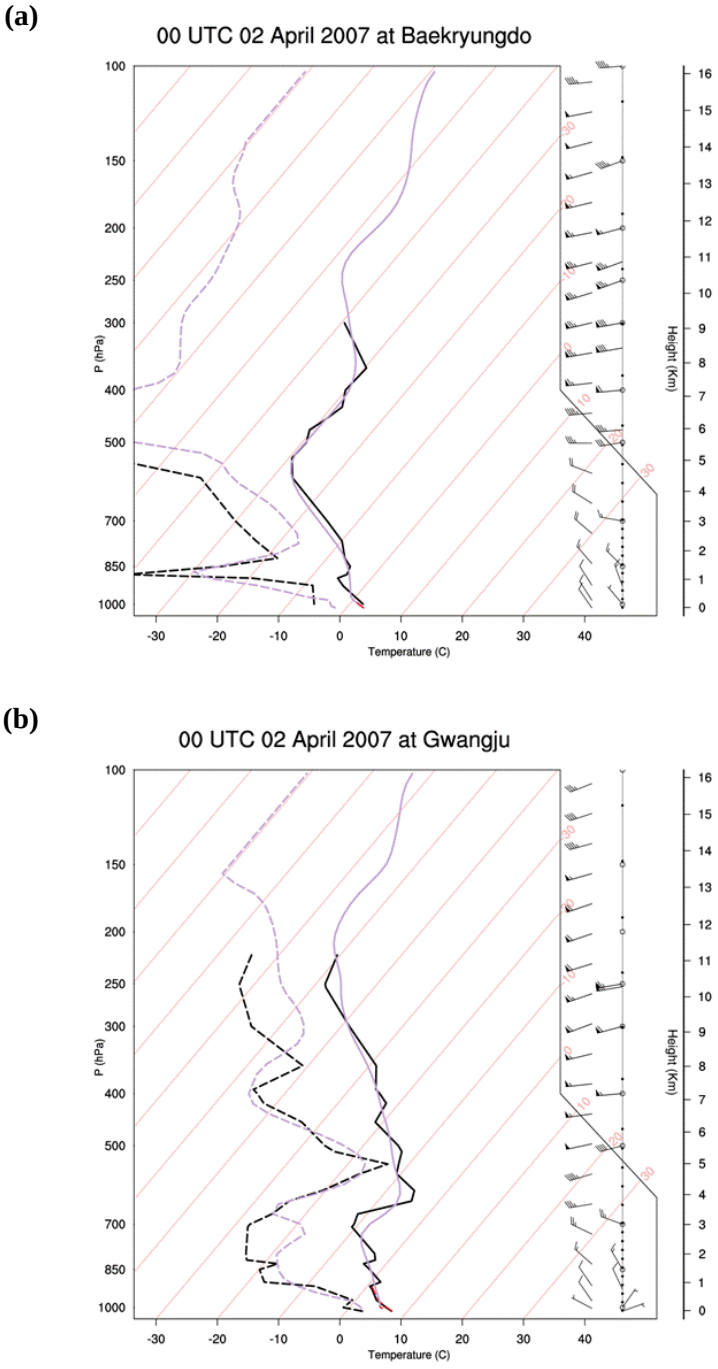

Fig. 5. Skew *T*-log *p* diagrams (temperature; solid, dewpoint; dashed) derived from the observed (black) and the simulated (gray) soundings at (a) Baekryungdo and (b) Gwangju observation sites in Korea at 00 UTC 2 April 2007. Simulated (right) and observed (far right) wind speeds at each level are shown in the right side of the diagram with full (10 m s^{-1}) and half (5 m s^{-1}) barbs and a pennant (50 m s^{-1}). Isotherms in 10 ºC intervals are denoted slantwise thin lines in both plots.

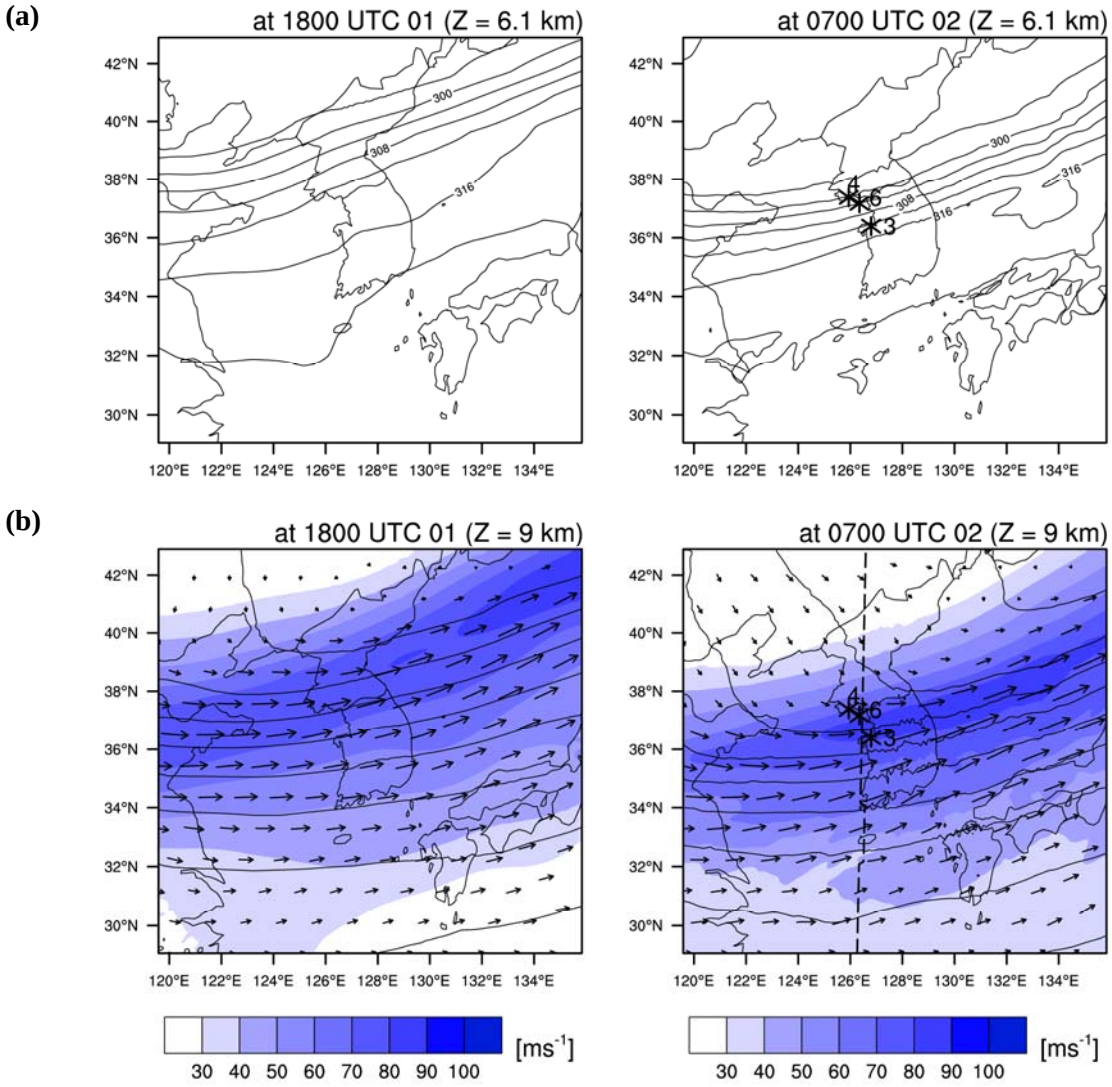

Fig. 6. Simulation results in domain 2: (a) potential temperature (contour) at Z = 6.1 km and (b) horizontal wind speed (shading) at Z = 9 km superimposed on wind vectors and pressure (contour) at Z = 6.1 km at 1800 UTC 1 April 2007 (left) and at 0700 UTC 2 April 2007 (right). Contour intervals of (a) and (b) are 4 K and 4 hPa, respectively. Locations of MOG-level CATs occurred around 0700 UTC 2 April 2007 in the west coast area are depicted with asterisks and corresponding numbers as denoted in Table 1.

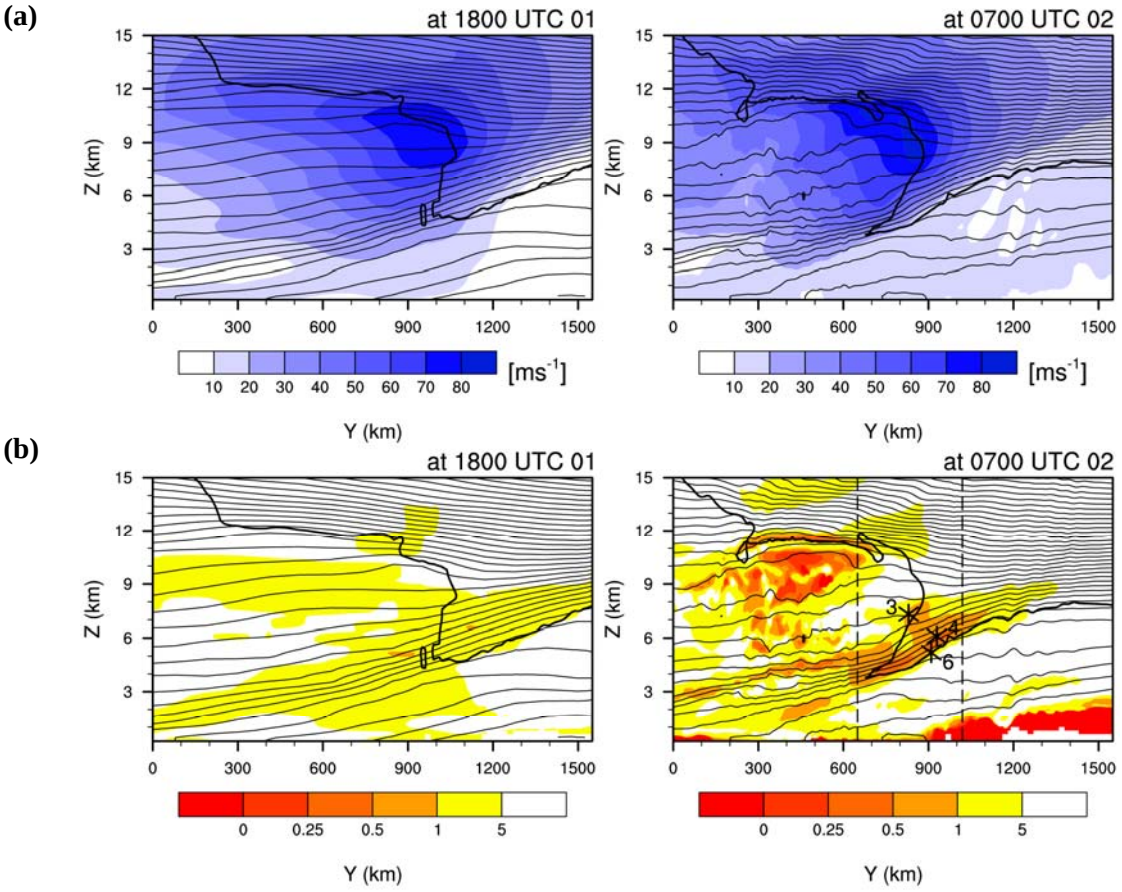

Fig. 7. Y-Z cross-sections of (a) horizontal wind speed (shading) and (b) local Richardson number (shading) superimposed with potential temperature (contour) and 1.5 PVU (potential vorticity unit; 10^{-6} K kg^{-1} m^2 s^{-1}; bold line) along the dashed line in Fig. 6b (right) derived using simulated results of domain 2 at 1800 UTC 1 April 2007 (left) and at 0700 UTC 2 April 2007 (right). Contour intervals in all plots are 2 K. Locations of MOG-level CATs over the west coast area of Korea are depicted with asterisks and corresponding numbers as denoted in Table 1.

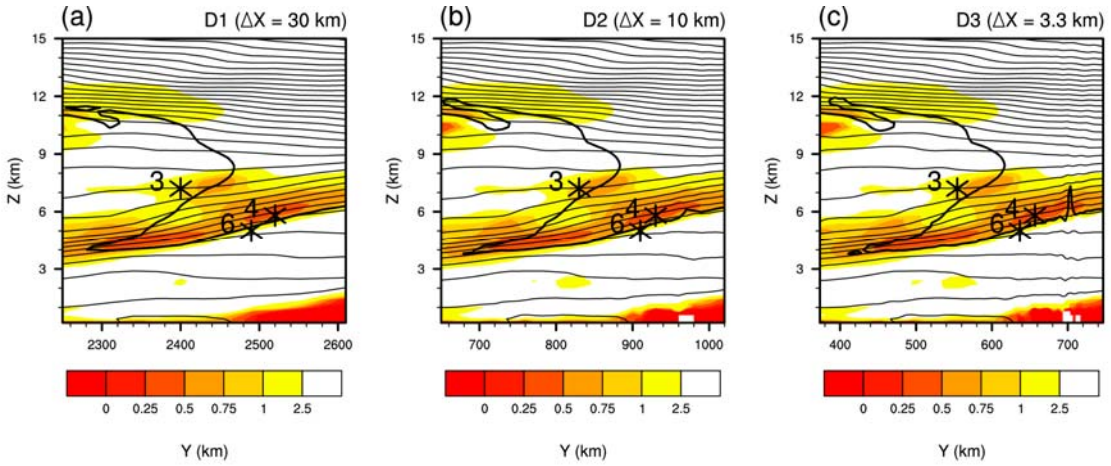

Fig. 8. Y-Z cross-sections of local Richardson number (shading) superimposed with potential temperature (contour) and 1.5 PVU (potential vorticity unit; 10^{-6} K kg^{-1} m^2 s^{-1}; bold line) in the region enclosed by two dashed lines at Y = 650 and 1020 km shown in Fig. 7b (right), derived using simulated results of (a) domain 1, (b) domain 2, and (c) domain 3, at 0700 UTC 2 April 2007. Contour intervals in all plots are 2 K. Note that the x-axis in each plot denotes the relative distance from the southernmost point of each domain. Locations of MOG-level CATs over the west coast area of Korea are depicted with asterisks and corresponding numbers as denoted in Table 1.

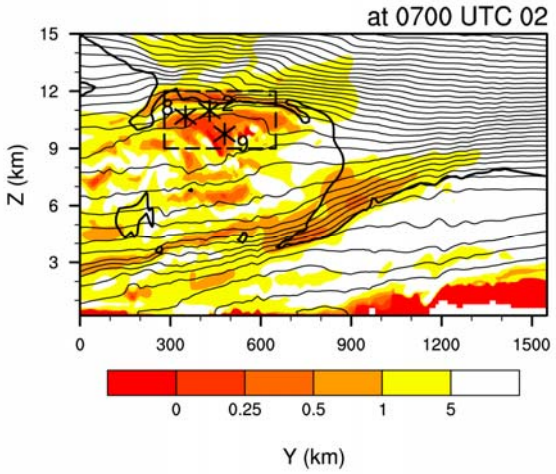

Fig. 9. The same as Fig. 7b (right) except that locations of MOG-level CATs over Jeju Island are depicted with asterisks and corresponding numbers as denoted in Table 1.

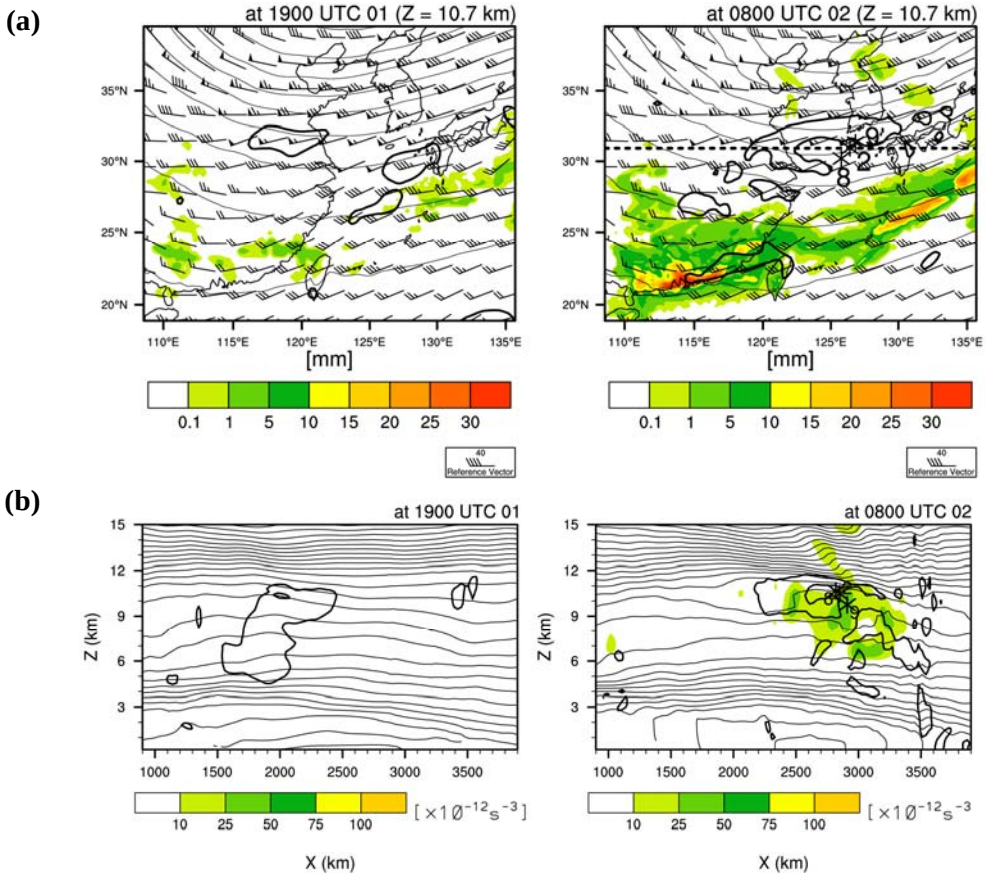

Fig. 10. Simulated results in domain 1 at 1900 UTC 1 April, 2007 (left) and at 0800 UTC 2 April, 2007 (right): (a) accumulated convective precipitation (shading) superimposed with horizontal wind barbs, pressure (contour), and zero absolute vorticity (bold line; s^{-1}) at Z = 10.7 km and (b) X-Z cross-sections of NCSU2 ($\times 10^{-12}\ s^{-3}$) superimposed with potential temperature (contour) and zero absolute vorticity (bold solid line) along the dashed line in (a).

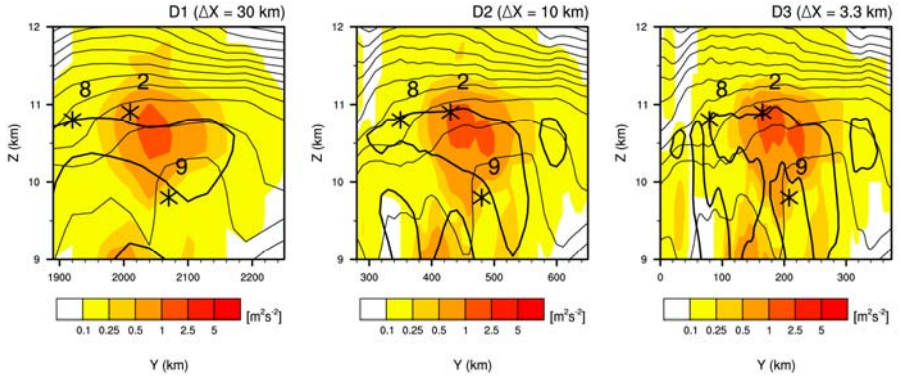

Fig. 11. Y-Z cross-sections of subgrid-scale TKE (shading; $m^2\ s^{-2}$) superimposed with potential temperature (contour) and zero absolute vorticity (bold line; s^{-1}) derived using simulated results of domain 1 (left), domain 2 (center), and domain 3 (right) focused on the dashed box in Fig. 9 at 0800 UTC 2 April 2007. Contour intervals in all plots are 2 K.

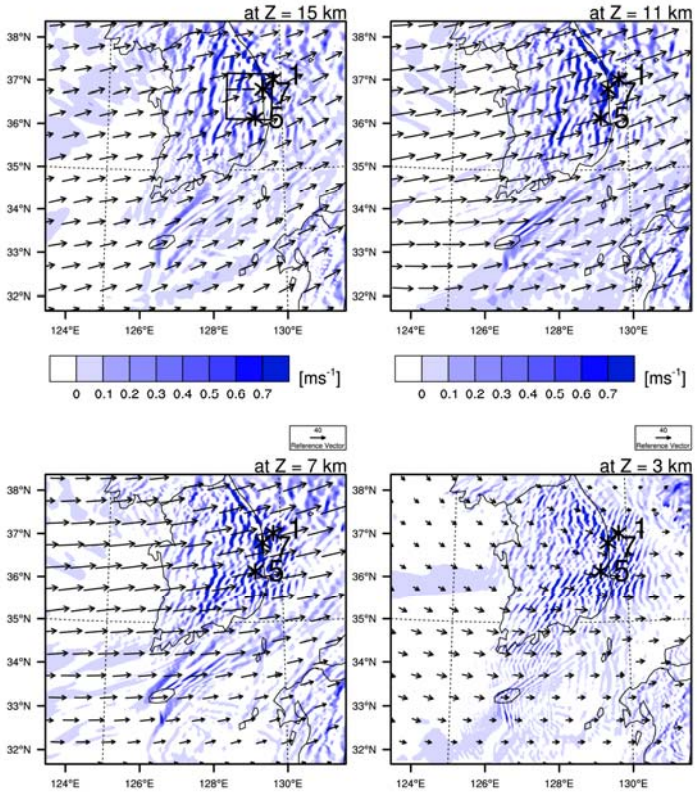

Fig. 12. Vertical velocity (shading; m s^{-1}) with horizontal wind vectors derived using simulated results of domain 3 at selected heights (Z = 15, 11, 7, and 3 km) at 0300 UTC 2 April 2007. Locations of MOG-level CATs over the eastern mountain area are depicted with asterisks and corresponding numbers as denoted in Table 1. Location of domain 6 is indicated as an inner box in the upper-left plot.

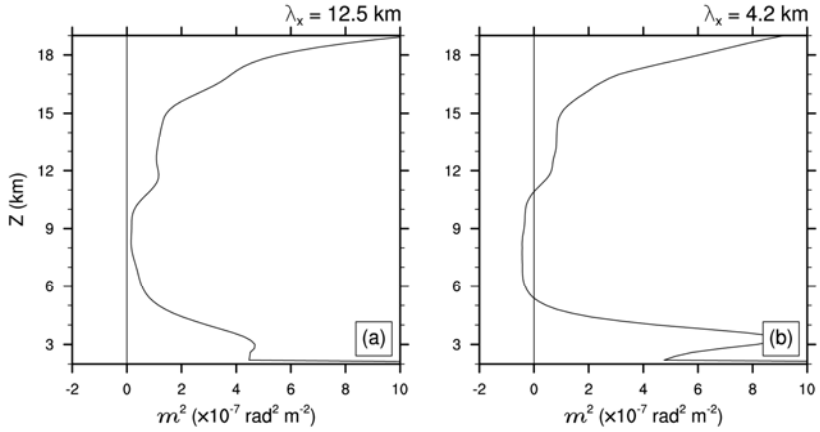

Fig. 13. Vertical profiles of m^2 (where m is the vertical wavenumber of the mountain wave) with horizontal wavelengths of (a) 12.5 km and (b) 4.2 km calculated using domain-averaged (domain 6) zonal wind and temperature at 0300 UTC 2 April 2007.

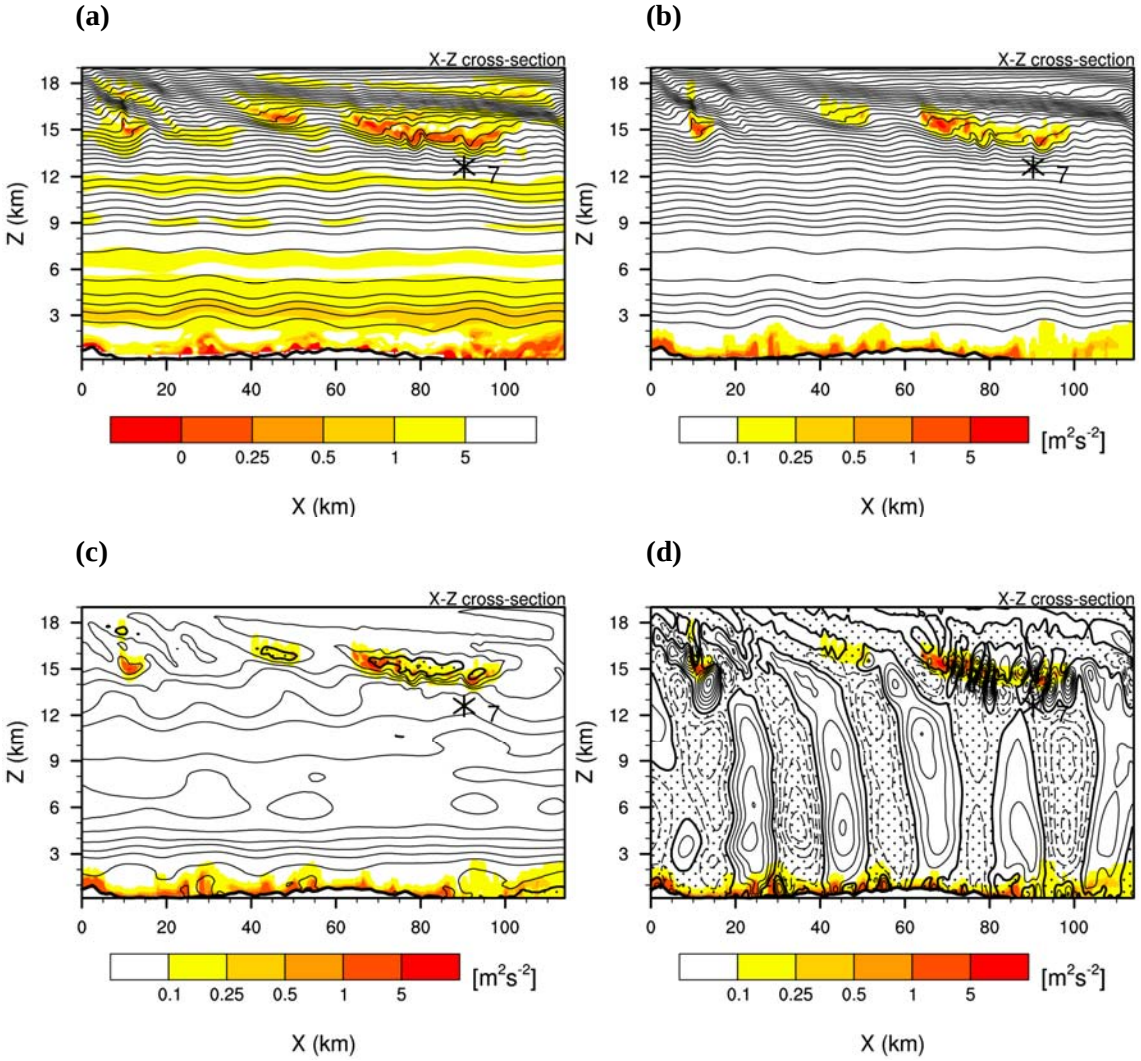

Fig. 14. X-Z cross-sections of potential temperature (K) superimposed on (a) Richardson number and (b) subgrid-scale TKE (turbulent kinetic energy; $m^2 s^{-2}$) and of (c) zonal wind (m s^{-1}) and (d) vertical velocity (m s^{-1}) superimposed on the subgrid-scale TKE derived using the simulated results of domain 6 at 0300 UTC 2 April 2007 along the line of Y = 75 km in domain 6 at which the No. 7 CAT is located. Zero and negative values of wind velocity in (c) and (d) are denoted by bold and dashed lines, respectively. Location of No.7 MOG-level CAT over the eastern mountain area is depicted with asterisk and corresponding number as denoted in Table 1.

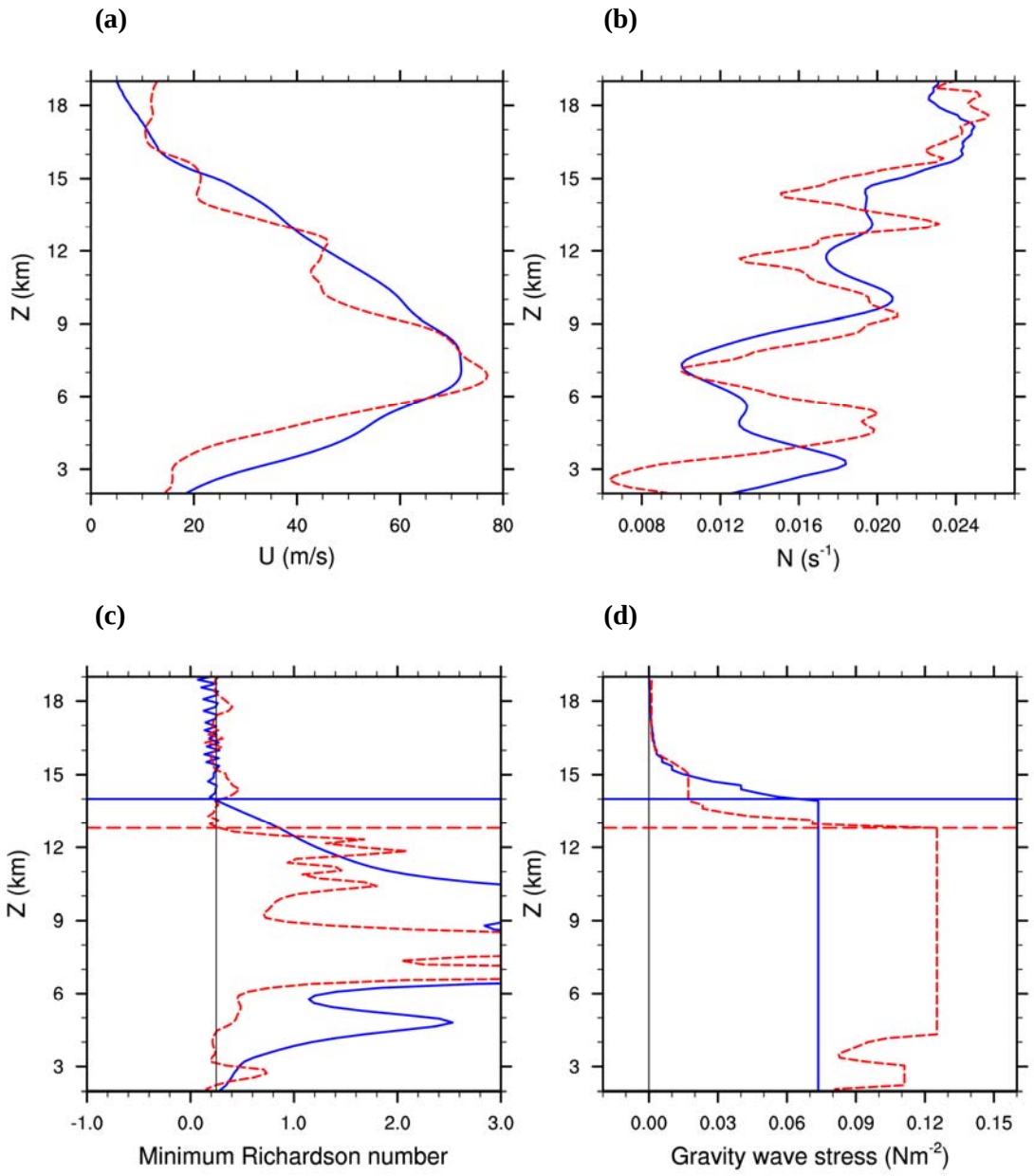

Fig. 15. Vertical profiles of (a) U (m s^{-1}), (b) N (s^{-1}), (c) minimum Richardson number, and (d) mountain-wave stress (N m^{-2}) derived using the simulated results from domain 6 (solid) and observed soundings at Osan station (dashed) at 0000 UTC 2 April 2007. Location of Osan station is depicted in Fig. 3b. Altitudes of wave breaking near the No.7 CAT estimated using the observed (dashed lines) and simulated (solid lines) soundings are depicted as horizontal lines in (c) and (d) plots.